PNAS RESEARCH ARTICLE | APPLIED PHYSICAL SCIENCES
APPLIED BIOLOGICAL SCIENCES

Gas-modulating microcapsules for spatiotemporal control of hypoxia

Thomas G. Molley[a,b], Shouyuan Jiang[c], Louis Ong[d,e,f], Chantal Kopecky[b], Chavinya D. Ranaweera[b], Gagan K. Jalandhra[a], Laura Milton[d,e], Egi Kardia[g,h], Zeheng Zhou[a,i], Jelena Rnjak-Kovacina[c], Shafagh A. Waters[g,h,i], Yi-Chin Toh[d,e,f,j], and Kristopher A. Kilian[a,b,h,1]

Edited by Catherine Murphy, University of Illinois at Urbana-Champaign, Urbana, IL; received October 17, 2022; accepted February 28, 2023

Oxygen is a vital molecule involved in regulating development, homeostasis, and disease. The oxygen levels in tissue vary from 1 to 14% with deviations from homeostasis impacting regulation of various physiological processes. In this work, we developed an approach to encapsulate enzymes at high loading capacity, which precisely controls the oxygen content in cell culture. Here, a single microcapsule is able to locally perturb the oxygen balance, and varying the concentration and distribution of matrix-embedded microcapsules provides spatiotemporal control. We demonstrate attenuation of hypoxia signaling in populations of stem cells, cancer cells, endothelial cells, cancer spheroids, and intestinal organoids. Varying capsule placement, media formulation, and timing of replenishment yields tunable oxygen gradients, with concurrent spatial growth and morphogenesis in a single well. Capsule containing hydrogel films applied to chick chorioallantoic membranes encourages neovascularization, providing scope for topical treatments or hydrogel wound dressings. This platform can be used in a variety of formats, including deposition in hydrogels, as granular solids for 3D bioprinting, and as injectable biomaterials. Overall, this platform's simplicity and flexibility will prove useful for fundamental studies of oxygen-mediated processes in virtually any in vitro or in vivo format, with scope for inclusion in biomedical materials for treating injury or disease.

hypoxia | microcapsules | biomaterials | stem cells | cancer

Significance

Cells in the body require precise tissue-specific oxygen levels varying from 1 to 14%. Specialized incubators are currently required to mimic these conditions and are not compatible with miniaturized multitissue cultures like body-on-a-chip devices. This article describes microscale capsules that facilitate spatiotemporal control of oxygen tension in cell culture. Key to this advance is an encapsulation procedure that yields the highest reported enzyme stability and activity within a microscale volume. We demonstrate how controlling oxygen affects cancer cell growth, organoid development, and formation of new blood vessels. Controlling capsule placement provides spatiotemporal gradients of oxygen-mediated tissue morphogenesis within single experiments. The flexibility of microcapsules provides scope for fundamental research and therapeutics where control of oxygen tension may have clinical utility.

Oxygen is one of the most important molecules that drives life on earth. For humans and other mammals, oxygen tension plays a critical role in aiding tissue development and maintaining normal tissue function, as well as pathological processes such as tumor development and progression (1). Low levels of oxygen in tissue is termed hypoxia, and hypoxic conditions mediate the transcriptional activity of hypoxia-inducible factors (HIFs) which regulate gene expression associated with multiple functional activities including angiogenesis, cell migration, differentiation, metabolism, and apoptosis (2, 3). These HIF proteins are sensitive to local oxygen tension which varies greatly within and between different tissues of the body (1, 4). While air has a saturation of around 20% oxygen, circulating blood levels sit around 5% (3), with various tissues such as gut, bone marrow, and cartilage reaching as low as 1% (5). These values contrast significantly from the 18.6% oxygen found in cell culture incubators (6), leading to cellular hyperoxia in vitro. For many years, developing a simple and efficient method to adjust oxygen tension in vitro has been a challenging task.

The most common practice for simulating low-oxygen conditions in vitro is the use of hypoxic incubators and hypoxic chambers. These devices control atmospheric oxygen levels and thus limit the amount of diffusible oxygen within the cell culture environment. However, their high cost makes them inaccessible to many researchers, and when cultures are inevitably removed from the incubator, cells are exposed to normoxic oxygen tension (7, 8). Furthermore, it is impossible to establish culture conditions that mimic the gradients of oxygen observed in tissue using hypoxic chambers. To overcome these issues, researchers have explored the use of chemical and enzymatic methods to create hypoxic environments. Baumann et al. first explored this concept in 2008 by using glucose oxidase paired with catalase to induce hypoxia in three different cancer cell lines (9). Further work also explored the use of laccase as an oxygen depletion enzyme to reduce the consumption of glucose from cell media (10). Critically, free enzymes are not stable long term in cell culture as they can readily be degraded by proteases. Therefore, to gain further oxygen control utilizing hydrogels, Gerecht and colleagues synthesized hydrogels with laccase covalently conjugated to the hydrogel polymer backbone to aid in enzyme stability (11). This technique has also been reported by Dawes et al. using glucose oxidase–immobilized hydrogels (12). While these systems enable greater control of local oxygen levels than hypoxic incubator/chambers, the methodology is specialized and limits the available selection of hydrogel networks. For the majority of cell and tissue cultures, there is little flexibility in the choice of matrix,

Author contributions: T.G.M., L.O., E.K., S.A.W., Y.-C.T., and K.A.K. designed research; T.G.M., S.J., L.O., C.K., C.D.R., G.K.J., L.M., E.K., Z.Z., and S.A.W. performed research; S.J., C.K., C.D.R., G.K.J., L.M., E.K., Z.Z., and J.R.-K. contributed new reagents/analytic tools; T.G.M., L.O., S.A.W., and Y.-C.T. analyzed data; and T.G.M., C.K., J.R.-K., S.A.W., Y.-C.T., and K.A.K. wrote the paper.

The authors declare no competing interest.

This article is a PNAS Direct Submission.

[1]To whom correspondence may be addressed. Email: k.kilian@unsw.edu.au.

This article contains supporting information online at https://www.pnas.org/lookup/suppl/doi:10.1073/pnas.2217557120/-/DCSupplemental.

Published April 11, 2023.

making this approach unsuitable for broad general use. Therefore, to broaden this concept's versatility, we sought an approach that could apply to any cell culture platform while utilizing the benefits afforded through enzymatic control of oxygen.

Here, we demonstrate a microscale gas-modulating system for spatiotemporal control over oxygen tension in cell culture. The microencapsulation system uses a gelatin microgel template with a polydopamine (PDA) coating, where tuning the coating polymerization alters the permeability and stability of capsules. Our approach led to unprecedented concentrations of enzyme, up to 40 mg/mL within the microcapsules, with stable activity maintained for over a month in cell culture conditions. We observed a dose–response in oxygen levels with enzyme concentration and demonstrated functional outcomes through reproducible control over stem cell and cancer cell functional activities. The uniform distribution of capsules led to stable oxygen tension in culture, while localizing the capsules to a single point led to oxygen gradients that were varied up to a centimeter in distance. Intestinal organoids cultured within the gradient showed spatiotemporal control of morphogenesis, demonstrating the ability to emulate tissue gradients in a single well. Furthermore, local attenuation of oxygen levels was shown to increase neovascularization from endothelial cells in two dimensions (2D), three dimensions (3D), and in ovo models, providing scope for these materials to be used in promoting in vivo angiogenesis. Overall, this work demonstrates a versatile system where gas-modulating capsules can be integrated with virtually any soft material system to locally control oxygen levels.

1. Results and Discussion

1.1. Characterization of PDA-Coated Gelatin Microparticles. Our method of oxygen reduction relies on the dual reaction of glucose oxidase paired with catalase. The glucose oxidase enzyme first oxidizes a glucose molecule, forming a gluconic acid and hydrogen peroxide molecule. Catalase in turn breaks two hydrogen peroxide down into two water molecules and an oxygen molecule. Together, this reaction reduces one dissolved oxygen (DO) molecule for every two glucose molecules (Fig. 1*B*). Previous use of this enzyme pair in vitro has been shown effective in creating hypoxia in cell culture conditions, but the free enzymes had poor stability and lost function within only 24 h of use (13). We hypothesized that microencapsulation of these two enzymes in a stable hydrogel environment would provide a simple yet effective method to prolong enzyme life and stability while maintaining efficacy. These capsules could then be added to culture systems in a variety of manners, e.g., purely in a solution, embedded in a cell-free gel that is in proximity to cells, embedded in a cell-laden bulk hydrogel, and even used as a component of a microgel scaffold (Fig. 1*C*).

For the capsule design, gelatin was chosen as the capsule core due to its low thermal gelation temperature. This enables easy microgel formation while preserving payload bioactivity. PDA was chosen as the capsule wall since it coats most materials with ease and has a pore size that is smaller than the enzymes but larger than glucose (pore diameters: PDA ~1 nm; glucose oxidase radius: ~6 nm) (14, 15). This enables diffusion of analytes in and out of the capsules while preventing enzymes from escaping or proteases from entering and degrading the enzymes. Once loaded, these capsules function as oxygen sinks that can easily be dispersed and spatial localized to regulate and manipulate oxygen tension (Fig. 1*A*). The kinetics of oxygen reduction can subsequently be tuned by varying either the number of embedded capsules or the concentration of enzyme within each capsule.

The microcapsule synthesis scheme using a water-in-oil emulsion method is shown in *SI Appendix*, Fig. S2. To maximize loading potential, cargo is added to the gelatin solution at a high concentration prior to addition to the oil bath. Importantly, previous methods to generate microgels of gelatin or gelatin methacryloyl (GelMa) with oil emulsions use acetone to dehydrate the particles prior to washing and collection (16, 17). Here, acetone will render loaded enzymes inactive. Therefore, the particles

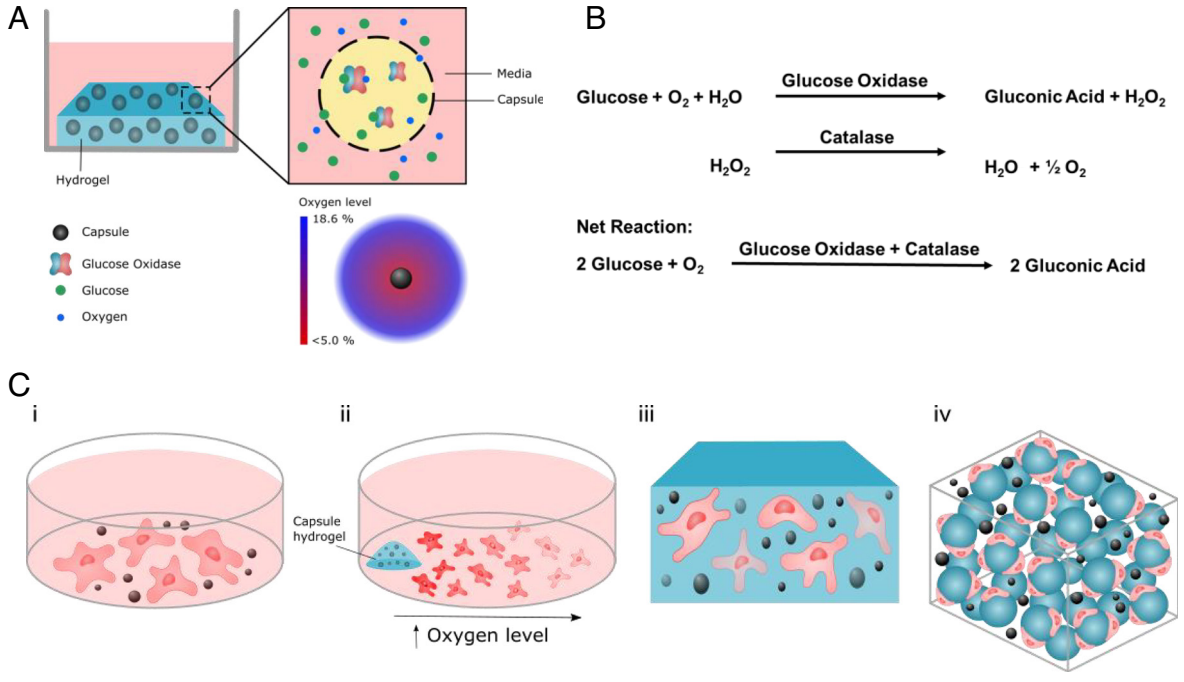

Fig. 1. Schematic of hypoxic capsules in microgels. (*A*) Schematic representation of glucose oxidase enzyme within a capsule. The enzymes are entrapped within the capsule walls, but the wall pore sizes are small enough to enable the exchange of enzyme substrates (glucose and oxygen). (*B*) Reaction scheme of glucose oxidase and catalase. (*C*) Schematic representations of capsules distributed in various formats: (*i*) uniformly dispersed in standard cell culture, (*ii*) spatial deposition for gradients, (*iii*) uniformly dispersed within a hydrogel, and (*iv*) distributed within granular media.

require a nonwater-miscible solvent to wash away excess oil. Hexane was chosen as it readily dissolves food oils while remaining immiscible with water (18). Optical images verify the formation of stable gelatin microgel particles without acetone dehydration (Fig. 2 *A*, *i*); scanning electron micrographs show smooth morphologies on the uncoated particle surfaces (Fig. 2 *A*, *ii*).

For the coating, dopamine hydrochloride (10 mg/mL) was added to a dilute suspension of gelatin microgels [10 w/v% particles in a Tris-HCl buffer (pH 8.5)] and shaken in a capless centrifuge tube to enable gas exchange. After 24 h, the particles adopted a brown/black appearance (Fig. 2 *A*, *iii*) corresponding to the color of PDA (19, 20). Scanning electron microscopy (SEM) showed a slightly rougher surface on coated particles (Fig. 2 *A*, *iv*), and size characterization revealed an average particle size of 60 ± 24 μm (Fig. 2*B*). Filtering can further reduce these capsule sizes, and microfluidics would enable the generation of capsules on the order of 1 μm. To determine the barrier functionality of the PDA coating, a permeation study was performed with gelatin microparticles coated for 0, 2, 4, or 24 h. The capsules were placed in a phosphate buffer saline (PBS) solution with fluorescein isothiocyanate (FITC)–labeled dextrans (250 kDa) for 24 h and subsequently imaged using confocal microscopy to

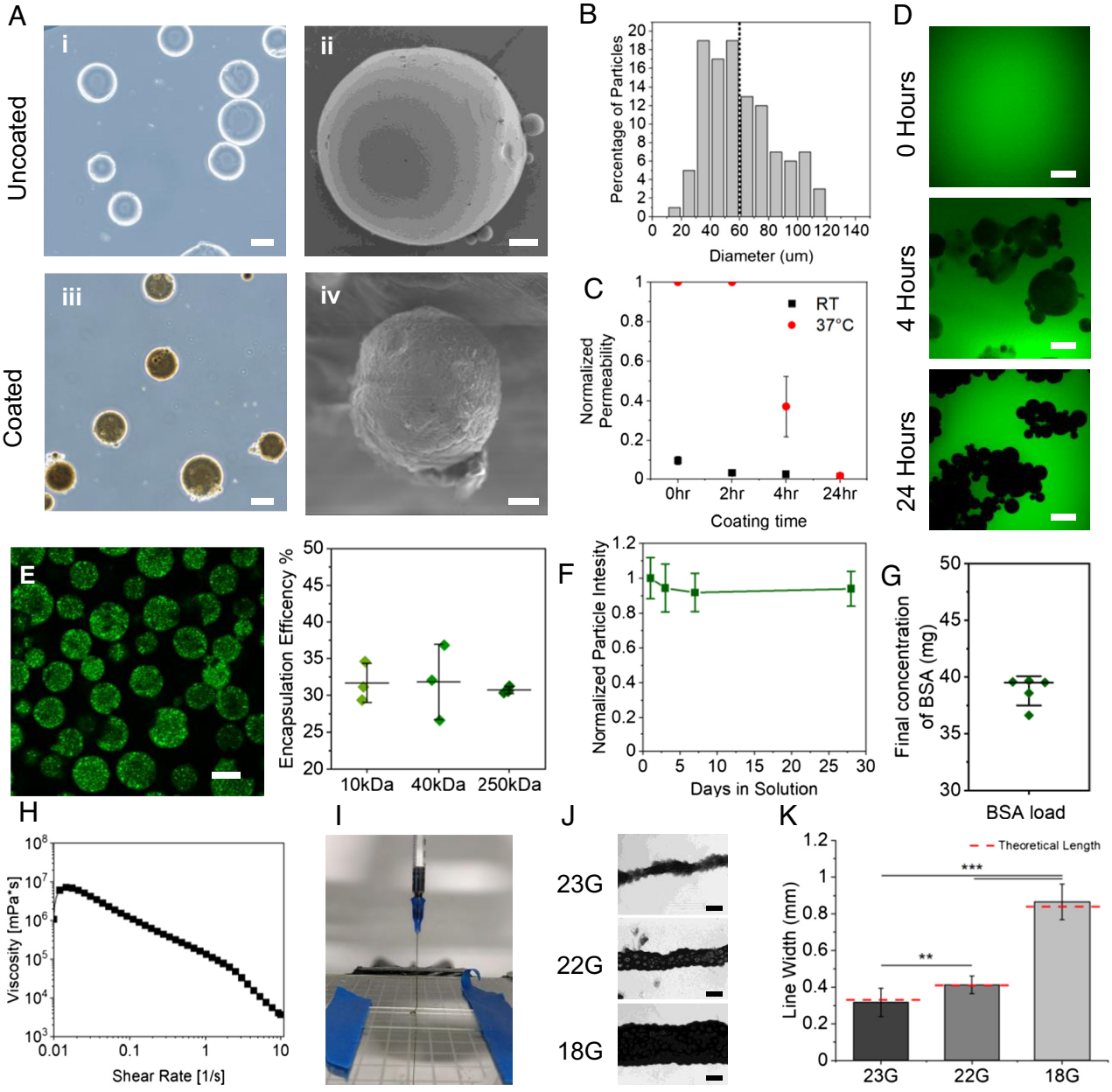

Fig. 2. Characterization of PDA gelatin microcapsules. (*A*, *i*) Bright-field microscopy images of uncoated gelatin microgels. Scanning electron microscope images of uncoated (*ii*) and PD-coated (*iv*) gelatin capsules. (*iii*) Bright-field microscopy image of polydopamine (PD)-coated gelatin microgels. (*B*) Size distribution histogram of uncoated gelatin microgels. (*C*) Normalized permeability of capsules based on fluorescence. (*D*) Confocal microscopy images of capsules (coated for 0, 4, or 24 h) sitting in FITC-dextrans for 24 h (37 °C). (*E*, *Left*) Confocal microscopy image of 24-h PD-coated microcapsules loaded with 250-kDa FITC-dextran (2 mg/mL). (*Right*) Plot of encapsulation efficiencies calculated for 10-, 40-, and 20-kDa dextrans. (*F*) Plot of normalized fluorescence intensity of FITC-BSA in microcapsules after 28 d. (*G*) Plot of the final concentration for 5 batches of BSA-loaded microcapsules. (*H*) Viscosity vs shear strain rate plot from shear strain sweeps (log ramp from 0.02 to 10 s^{-1}). (*I*) A photograph of a printed continuous line filament of jammed microcapsules. (*J*) Bright-field microscopy images of jammed microcapsule printed lines with various nozzle sizes (23, 22, and 18G). (*K*) A plot of analyzed microcapsule line diameters with varied nozzle dimeters. Red lines indicate the inner diameter of the nozzles used. (Scale bars, 300 μm.) [Scale bars, 10 μm (*A*, *ii* and *iv*), 50 μm (*A*, *i* and *iii*), (*E* and *J*) 300 μm.] $^{**}P < 0.01$, $^{***}P < 0.001$, one-way ANOVA. Error bars represent SD.

measure capsule fluorescence at 20 and 37 °C. There was a noticeable decrease in capsule fluorescence as coating time increases for the 20 °C condition; however this difference was minimal (*SI Appendix*, Fig. S3 *A* and *B*). When assessing the 37 °C condition, it became clear that stable coatings did not occur until after 4 h of coating (Fig. 2 *C* and *D*). Even after 4 h, faint silhouettes of capsules can be seen with a significant difference in fluorescence when compared to the room temperature condition ($P < 0.0001$), suggesting a leaky coating. However, after coating for 24 h, there is a slight difference in permeability between the two temperature conditions. To verify that the porosity of the capsules was small enough to enable oxygen and glucose diffusion, capsules were suspended in a solution of fluorescein (332.31 Da) for 1 h and subsequently washed and imaged. Light intensity was found to increase within 5 s (*SI Appendix*, Fig. S3 *C* and *D*), suggesting large enough pores for analyte diffusion. Therefore, 24-h coatings were subsequently used for the rest of the work.

To evaluate encapsulation efficiency, capsules were synthesized with FITC-dextran (2 mg/mL of 10, 40, or 250 kDa) and without dopamine coating, followed by shaking for 4 h to simulate the coating procedure (Fig. 2*D*). Dextrans were chosen as they are a common model for molecular diffusion due to their similar isoelectric points and physical characteristics at all sizes. Confocal microscopy images of capsules loaded with 250-kDa dextrans were first used to confirm loading (Fig. 2*E*). The uncoated capsules were then collected, washed, and melted. A fluorescence spectrophotometer was used to measure the amount of FITC-dextran with an emission maximum of 517 nm. To quantify the dextran concentration, standard curves of FITC-dextrans at varied concentrations were made for each size (10, 40, and 250 kDa) (*SI Appendix*, Fig. S4 *A–D*). Confocal microscopy images of capsules loaded with 250-kDa dextrans were first used to confirm loading (Fig. 2*E*). The encapsulation efficiencies for 10-, 40-, and 250-kDa dextrans were 32 ± 2%, 32 ± 4%, and 30 ± 0.5%, respectively (Fig. 2*E*). Material loss most likely occurs during the coating process before a sufficiently thick enough coating is formed.

To measure the long-term stability of the coatings, FITC-labeled bovine serum albumin (BSA) molecules were loaded into capsules and stored at 4 °C. These capsules were subsequently imaged under a confocal microscope over 28 d (*SI Appendix*, Fig. S4*C*). To combat the gradual photobleaching of FITC, the internal particle fluorescence was normalized to a solution of free FITC-BSA stored under the same conditions. A 94 ± 1% retention in fluorescence is seen over the 28 d (Fig. 2*F*). To test the maximal loading capacity of our capsules, 10 wt% BSA (with 0.1% being FITC-BSA) was added to the gelatin precursor solution. A similar procedure to the encapsulation efficiency was performed on supernatants of dissolved uncoated capsules after 4 h (*SI Appendix*, Fig. S5*A*). A standard curve was made for the FITC-BSA (*SI Appendix*, Fig. S5*B*) which gave a final BSA concentration of 39 ± 2 mg/mL (39% BSA, wet weight) (Fig. 2*G*). To our knowledge, this is the highest loading of bioactive molecules in a microcapsule to date (21–28). Microscale hydrogels have been widely used as delivery vehicles, scaffolds, and support matrices for biofabrication (29, 30). Considering the microcapsules are of a similar size, integrating capsules within a jammed suspension of microgels could provide localized control of oxygen during biofabrication. To determine if the microcapsules would behave similarly to microgels, we performed parallel plate rheology on jammed suspensions of the microcapsules, which demonstrated similar shear-thinning behavior (Fig. 2*H*) with a yield stress value of 40 Pa (*SI Appendix*, Fig. S6*A*). To demonstrate reversibility of their jammed state, 2-min intervals of high (200%) and low (0.2%) strain were applied cyclically. Here, the jammed capsules can be seen to recover full mechanical stiffness near instantaneously for multiple continuous cycles (*SI Appendix*, Fig. S6*B*). To assess injectability, jammed microcapsules were loaded into 1-mL syringes and extruded into lines (Fig. 2*I* and Movies S1–S3) (31). A fidelity assessment of 3D printed lines demonstrates high control of the line with widths varying from 300 to 800 μm, with the average capsule line width diameter less than 5% from the nozzle's inner diameter (Fig. 2 *J–K*). These studies demonstrate how microcapsules can be used in multiple formats from single particles to high-density suspensions for syringe injection and biofabrication.

1.2. Glucose Oxidase–Loaded Capsules Reduce DO Levels. We next evaluated the ability to load functional enzyme into the microcapsule system. First, glucose oxidase was loaded into microgel capsules (1 U/mL). A glucose oxidase activity kit with a fluorescent reporter was used to measure the hydrogen peroxide production activity of enzyme-loaded microcapsules. Capsules (20 mg/mL) were added to wells in a plate reader, and the fluorescent output (517 nm) was measured every 3 min for 45 min. When measuring the activity around the capsules over time, the enzyme activity reached a plateau after 3 to 6 min (Fig. 3*A*). This is likely due to initial diffusion constraints as glucose substrates and peroxides need to freely diffuse into and out of capsules. After 45 min, capsules loaded with 1 U/mL glucose oxidase had an activity of 46 mU/mL, providing a functional encapsulation efficiency of 5% (Fig. 3*B*). This discrepancy between these values and the 30% found for loaded BSA may be due to loss of functionality of some of the encapsulated enzymes during encapsulation and coating at elevated pH (~8.5). The substrates and products of the reaction, namely glucose and oxygen, also need to diffuse through the capsule wall for measurement which can limit the reaction rate and the perceived activity. In addition, immobilized enzyme activity can decrease by up to 80% when compared to free enzyme (32). This underscores the importance of an encapsulation system with high cargo loading capacity.

Glucose oxidase is known for having a high shelf life under proper storage conditions (33, 34). To measure the shelf life of the enzyme-loaded capsules at 4 °C in PBS, a batch of capsules had activity measured at 1, 3, 7, 14, and 21 d after synthesis. No noticeable difference in glucose oxidase activity was found after 21 d in storage demonstrating high stability (Fig. 3*C*). Next, glucose oxidase–loaded capsules were stored in cell culture media (Dulbecco's Modified Eagle Medium (DMEM)) at 37 °C for 5 wk along with a solution of free enzyme as a control. After 1 wk, the capsules lost only 11 ± 0.3% of enzyme activity ($P = 0.0094$), whereas the free enzyme had a reduction in activity of 84.4 ± 0.1% ($P < 0.0001$). After 5 wk, the capsules lost only 34 ± 0.4% of enzyme activity ($P < 0.0001$), whereas the free enzyme had lost 99 ± 0.2% of enzyme activity ($P < 0.0001$). Together, these results demonstrate how our microencapsulation system yields excellent enzyme stability providing a tool that could maintain hypoxic cell cultures for weeks.

With confirmation that capsules loaded with glucose oxidase can generate hydrogen peroxide, we next aimed to verify that encapsulated glucose oxidase, along with catalase, can reduce oxygen levels. For all tests, catalase was loaded at a functional activity of 60 times that of glucose oxidase. This ratio is to ensure that hydrogen peroxide produced by glucose oxidase is immediately extinguished by the catalase. This ratio is also consistent with previous work using enzymes to create hypoxic cell culture environments (9, 13). To best simulate the oxygen level conditions for cell culture conditions, a DO probe was placed 7 mm deep (the depth of our hydrogels in a 24-well plate with 1 mL of liquid) into a 12-well plate loaded with 4 mL of cell culture media

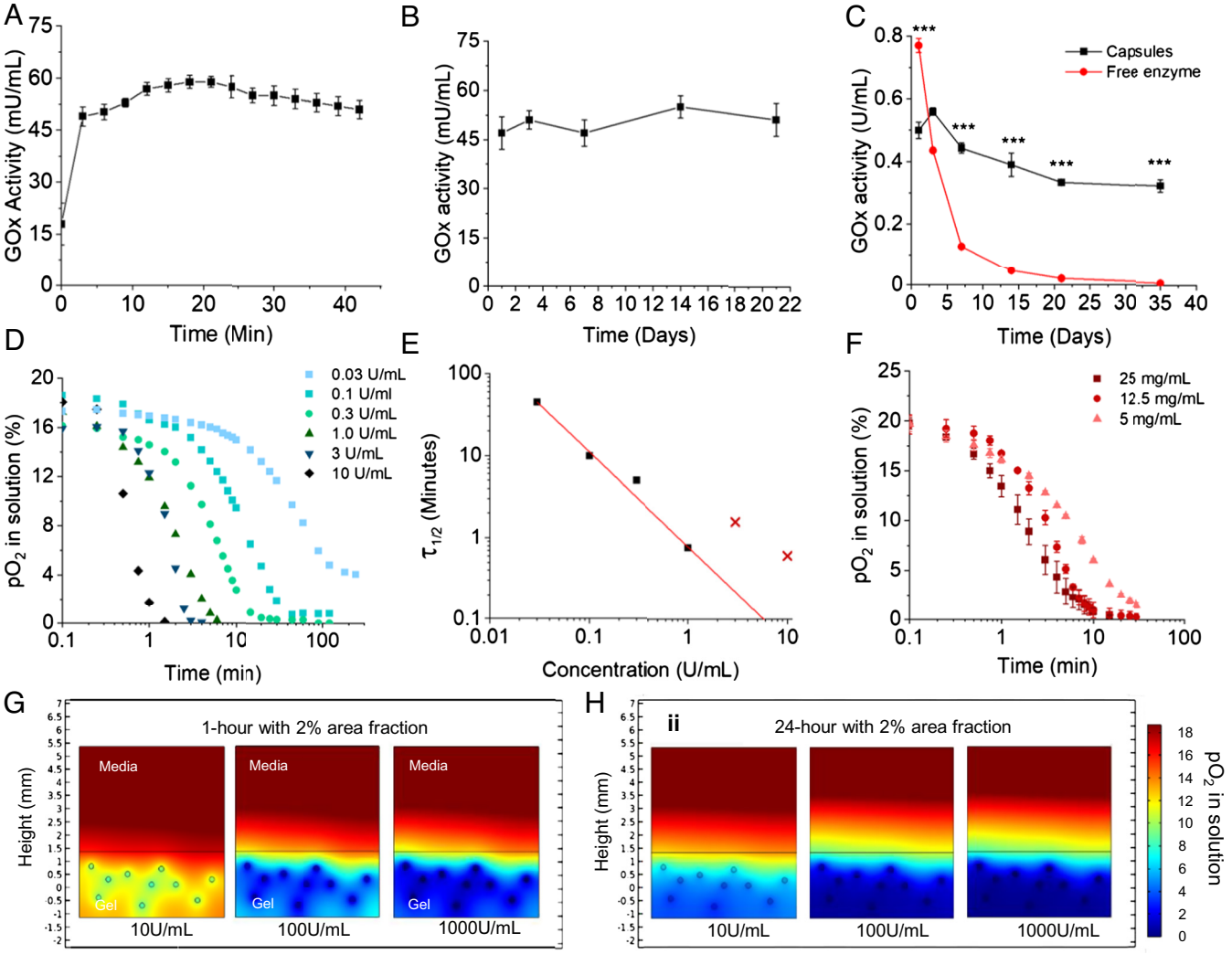

Fig. 3. Characterization of glucose oxidase activity in capsules. (*A*) Glucose oxidase (GOx) activity overtime for glucose oxidase–loaded microcapsules (1 U/mL) measured with a glucose oxidase activity kit on a plate reader with 517-nm emission. (*B*) Long-term activity of glucose oxidase capsules stored at 4 °C in between measurements. (*C*) Long-term activity of glucose oxidase capsules and free enzyme stored at 37 °C in between measurements. (*D*) Plot of the dissolved oxygen partial pressures for varied concentrations of glucose oxidase (with a 1:60 ratio with catalase) in cell media at room temperature. (*E*) Plot of the saturation halftime versus glucose oxidase concentration. The two x's correspond to data points that were not used for the linear fit. (*F*) A plot of the dissolved oxygen partial pressures for capsules at varied concentrations (5, 12.5, or 25 mg/mL of glucose oxidase–loaded capsules (1,000 U/mL, 60,000 U/mL catalase)). (*G* and *H*) Modeling the kinetics of oxygen diffusion of varied capsule concentrations at 1 h (*G*) and 24 h (*H*). Data are presented as average of n > 3 repeats with SD. ***$P < 0.001$, one-way ANOVA.

(*SI Appendix*, Fig. S1). A 6-mm stir bar was added to the well and rotated at 250 rpm to ensure enough fluid flow at the probe interface for accurate measurement while preventing disruption of the air–liquid interface. All measurements were performed at 21 °C. When testing at room temperature and pressure, the probe baseline read 9.07 mg/L of oxygen which, when using Henry's law, gives a partial pressure of 21.0% oxygen. The DO levels were measured for glucose oxidase concentrations of 0.03, 0.1, 0.3, 1, 3, and 10 U/mL. As expected, the DO levels were found to decrease as the glucose oxidase concentration increased (Fig. 3*D*). At each concentration, the oxygen saturation versus time relationship follows a sigmoidal curve shape. As the added enzymes first begin removing oxygen, there is a slight delay before the probe can register the reduction. And once the oxygen levels begin reaching lower saturation levels (<1%), the enzymes begin to compete with the oxygen diffusion from the air–liquid interface. This is most apparent when comparing the 10 U/mL sample versus the 0.03 U/mL. Since some solutions do not reach 0% saturation, a different metric is needed for comparison between concentrations. Here, we define the saturation halftime. This halftime is the time required for the DO levels in a solution to reach half (10.5% pO_2) of atmospheric oxygen concentration (a pO_2 of 21%). The halftimes for each solution were plotted against the concentration of glucose oxidase to create a standard curve. The halftime activity relationship followed a power law model with high accuracy (R square = 0.995) for activities of 1 U/mL and below (Fig. 3*E* and *SI Appendix*, Fig. S7*C*). Notably, the 3 and 10 U/mL solutions did not decay fast enough due to the limitation in speed of our oxygen probe. Therefore, they were not used for the best-fit equation.

To measure the effect of catalase on the solution, pure glucose oxidase (0.3 U/mL activity) without catalase was added to the microcapsules. Here, the sample without catalase shifted the activity curve to the left, suggesting faster oxygen depletion. Calculation of the saturation halftime gives 5.8 and 3.5 min, a 40% reduction, for the catalase and catalase-free conditions, respectively (*SI Appendix*, Fig. S7 *A* and *B*). This fits with our expectations as catalase should lead to a reduction in oxygen depletion by 50%. Glucose oxidase–loaded and catalase-loaded microcapsules of varied activities (1,000 U/mL glucose oxidase and 60,000 U/mL catalase; 5, 12.5,

and 25 mg/mL of capsules) were subsequently added to the same DO probe setup to measure the effect of encapsulation on activity. These capsules all reached hypoxic levels of oxygen tension (<5% pO_2) by 15 min, with a saturation halftime of 1.9 ± 0.4, 3.0 ± 0.3, and 5.9 ± 0.6 min for the 5, 12.5, and 25 mg/mL conditions, respectively (Fig. 3*F*).

To test the viability of capsules within granular media toward controlling oxygen during biofabrication, a capsule-loaded GelMA microgel suspension (2 vol% capsules in the gel, 0.4 mL of hydrogel volume; final of 2 mg/mL of capsules) was analyzed with the identical setup. These loaded microgel suspensions had a saturation halftime of 23 min, reaching a plateau of 2% oxygen saturation after 2 h (*SI Appendix*, Fig. S7*D*). These data suggest that hypoxic conditions can readily be reached with a low total volume fraction of capsules. One caveat with this methodology is that it can only read the oxygen levels in a solution. It is well appreciated that both in vitro hydrogels and in vivo tissues can lead to reduced oxygen levels when thick enough (35). Additionally, even slight differences in depth of cell culture medium in flasks and wells can affect the oxygen levels to adherent cells (6, 36). Therefore, the measurements of liquid at the surface likely underestimate the levels of hypoxia that cells experience within the microgel suspensions. Nonetheless, these measurements provide insight into the upper bound of glucose oxidase needed to establish these conditions.

To support our experimental results, we employed a mathematical model using COMSOL and Michaelis–Menten kinetics with O_2 as the analyte as previously described (37). The oxygen levels in hydrogels loaded with 2% volume fraction of capsules, containing 10, 100, or 1,000 U/mL of enzyme, were modeled over 24 h. After 1 h, more than 80% of the 1,000 U/mL gel can already be seen at hypoxic levels (<5% O_2), whereas the 100 U/mL condition is closer to 6 to 10%, and the 10 U/mL condition is closer to 10 to 15% (Fig. 3*G*). By 2 h, the 100 U/mL condition stabilizes below 5%, plateauing at between 2 and 3% by the 6th hour (*SI Appendix*, Fig. S8*A*). By 24 h, the 10, 100, and 1,000 U/mL conditions have all stabilized, given midplane oxygen levels around 5, 2, and 0.2%, respectively (Fig. 3*H*). These results suggest that tuning the loaded enzyme concentration can provide control over the final level of oxygen in cell culture conditions. To measure the effect of capsule concentration, additional models were performed of both 0.5% volume fraction and a single capsule. Even at 0.5% volume fraction, a hypoxic level can be maintained evenly underneath the top plane of capsules (*SI Appendix*, Fig. S8*B*). However, the range of hypoxia afforded by a single capsule at 1,000 U/mL is limited to only a distance of 200 μm. This indicates that there is a baseline concentration of capsules (a 0.5% volume fraction at most) needed to maintain homogeneous oxygen levels. In addition, this suggests that sequestering and spatially controlling capsule locations could enable the formation of oxygen gradients.

1.3. Control of Oxygen Regulates Hypoxic Signaling in Stem Cells and Cancer Spheroids. Next, we investigated the effect of hypoxia mediated by functioning oxygen-modulating microcapsules on cell viability. Live dead assays were performed on days 1 and 5 for 3 cell lines: A375-P (human melanoma), adipose-derived stromal cells (ADSCs), and human umbilical vascular endothelial cells (HUVECs). Capsules loaded with 1,000 U/mL glucose oxidase and 60,000 U/mL catalase were added to GelMa microgel suspensions used previously (38), (2 vol% of capsules) along with one of the cell lines (*SI Appendix*, Fig. S9). Here, 1,000 U/mL inside the capsules would give 2 U/mL in total solution in the well of a 24-well plate. With a 5% enzyme functionality, this provided a rough activity of 100 mU of glucose oxidase activity in one well (1 mL volume). Since all following in vitro studies were performed in 24-well plates with 1 mL of media, all future references of U/mL of enzyme will refer to the initial loading within the capsules for consistency.

After 1 d, there was a reduction in viability for the melanoma cell line from 97 ± 1% to 65 ± 20% when hypoxic capsules were added. Meanwhile, the ADSCs and HUVECs showed little difference (*SI Appendix*, Fig. S9 *A* and *B*). By 5 d, nearly all A375-P cells were dead (16 ± 12%, $P = 0.000017$), while HUVECs had a drop in viability to 36 ± 20% ($P = 0.0016$) (*SI Appendix*, Fig. S9*C*). Surprisingly, the ADSCs showed no decrease in viability even after 5 d (93.7 ± 0.3 versus 92.5 ± 5.5%, $P = 0.999$). However, the ADSCs, along with the HUVECs, showed spreading in the control condition but no noticeable cell spreading in the glucose oxidase condition (*SI Appendix*, Fig. S9*A*). Data from the DO probe showed that these capsules exhibit an activity of around 0.3 U/mL which gives a <1% oxygen saturation after 20 min at the surface of the gel. Thus, while some cells may survive at this level of hypoxia, cell spreading and proliferation are significantly impaired.

To explore the effect of hypoxia on intracellular HIF1-alpha (HIF1-α), microgel suspensions were loaded with ADSCs (1×10^6 cells per mL) with either no capsules or capsules with 100, 250, or 1,000 U/mL glucose oxidase (2 vol%; 6,000, 24,000, or 60,000 U/mL catalase, respectively). At both days 1 and 3, significant expression of HIF1-α can be seen in the capsule conditions but not in the control (Fig. 4*A*). Here, the control sample had 7.5 ± 3.5% of cells with expression, while the 1000 U/mL glucose sample had 73 ± 11% (P = 0.0013) (Fig. 4*B*). Moreover, hypoxia has been shown to have an effect on the extracellular vesicle (EV) output of mesenchymal stem cells (39, 40), To measure if our capsule-induced hypoxia had any effect on ADSC EV output, ADSCs were embedded into 3D microgel suspensions with capsules containing 0, 30, or 250 U/mL glucose oxidase (1×10^6 cells per mL, 2 vol% capsules in hydrogel). After 72 h in serum-free media, the supernatants were collected, and the EVs were isolated and analyzed. No differences were found in the concentration of exosomes across all three conditions (Fig. 4*C*). However, there was a significant increase in mean vesicle diameter for the hypoxic condition compared to the control ($P = 0.010$) (Fig. 4 *D* and *E*). This correlated well with previously reported work (41). The presence of CD9, a known surface marker for exosomes, in the EVs was also confirmed via western blots (*SI Appendix*, Fig. S10). Overall, these data suggest that the ADSCs may indeed be experiencing and responding to the low-oxygen environment, leading to changes in the secretion of EVs.

When sufficiently large enough, all cancerous tumors exhibit hypoxic cores (42). Aberrant tumor paracrine signaling networks disrupt nearby vasculature, leading to leaky vessels and poor nutrient and oxygen delivery. This disruption can generate hypoxic cores with a tumor volume as they continue to grow. These hypoxic cores have been implicated in tumor progression, including higher cancer cell survival, aggressiveness, and a more frequent incidence of metastasis (42–44). Therefore, model systems that can replicate hypoxic microenvironments in the laboratory are important tools for fundamental research and drug development.

To measure the effect of hypoxia on melanoma cells, we embedded A375-P human melanoma cells in GelMA microgel suspensions (between particles) with a filler of 1 wt% GelMA in the microgel interstitial space. These suspensions were subsequently loaded with microcapsules that contained 0 or 100 U/mL glucose oxidase (and 6,000 U/mL catalase)—10% of the enzyme activity that led to total cell death of the A375-P cells in the live dead study. In the control condition, A375-P cells can be seen to grow in clusters that expand in size by 55% ($P = 0.07$) over the course

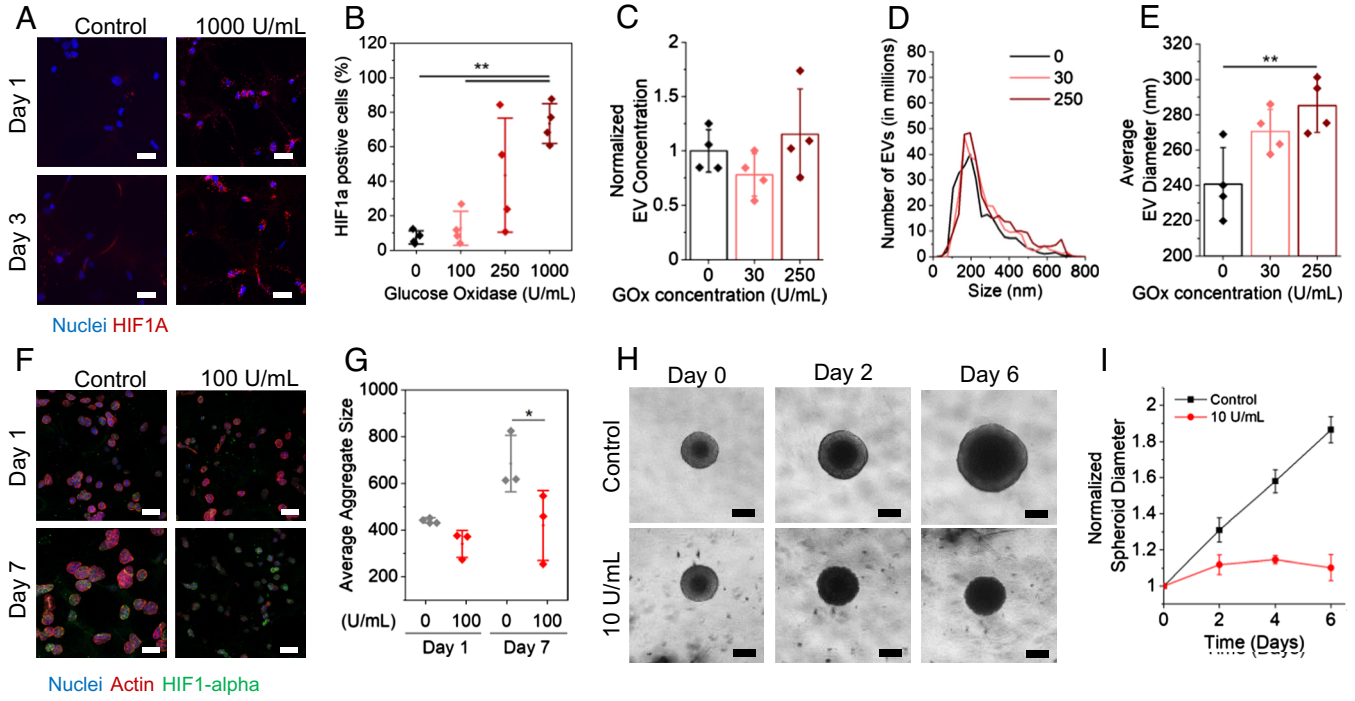

Fig. 4. Effect of hypoxia on ADSCs and tumor cells. (*A*) Confocal z-stack projections of ADSCs (1×10^6 cells per mL) stained with Hoechst (nuclei, blue) and HIF1-alpha (red) after 1 or 3 d in culture in microgel suspensions (10 wt%, 1% filler) with or without 2 vol% of glucose oxidase capsules (1,000 U/mL, 60,000 U/mL catalase). (*B*) Cell counts per replicate region of HIF1-alpha-positive cells for each of the glucose oxidase concentrations (capsules loaded with 0, 100, 250, and 1,000 U/mL). Concentrations (*C*), size plots (*D*), and average diameters (*E*) of EVs isolated from ADSCs in microgel suspensions with capsules loaded with varied glucose oxidase concentrations. (*F*) Confocal z-stack projections of A375-P cells stained with Hoechst (nuclei, blue), phalloidin (actin, red), and HIF1-alpha (green) after 1 or 7 d in culture in microgel suspensions (medium, 10 wt%, 1% filler) with or without 2 vol% of glucose oxidase capsules (100 U/mL, 6,000 U/mL catalase). (*G*) Plots of average A375-P aggregate size per replicate overtime. (*H*) Optical images of MCF7 breast cancer spheroids embedded in Geltrex over 6 d with no capsules or with capsules loaded with an equivalent of 10 U/mL. (*I*) Growth curves of breast cancer spheroid diameters. [Scale bars, 50 μm (*A* and *F*), 200 μm (*H*).] n ≥ 3 **P* < 0.05, ***P* < 0.01, one-way ANOVA. Error bars represent SD.

of 7 d (Fig. 4*F*). In contrast, the cell clusters in microgel suspensions with hypoxia-inducing capsules increased in size by only 23% ($P = 0.77$) and 61 ± 20% the size of the control condition ($P = 0.049$) (Fig. 4*G*). We next explored the influence of hypoxia on tumor spheroids to evaluate this commonly used tumor model. Here, MCF-7 breast cancer spheroids were embedded into Geltrex with 0, 10, 30, or 100 U/mL capsules loaded. For the conditions with 30 or 100 U/mL capsules, the spheroids did not proliferate during prolonged culture. For the 10 U/mL condition, there was slight growth through the first 2 d, after which the spheroids died (Fig. 4 *H* and *I*). These findings were replicated when using a more aggressive breast cancer cell line, MDA-MB-231, where there was little tumor growth for the hypoxic condition over 6 d (*SI Appendix*, Fig. S11). Together, our findings suggest that tumor cells within our in vitro models were sensitive to hypoxia, leading to HIF1-α signaling and apoptosis, thereby providing a model to emulate the effect of hypoxia in cancer cell culture.

1.4. Spatial Patterning of Microcapsules Provides Oxygen Gradient to Direct Intestinal Organoid Morphogenesis. A key advantage of using microcapsules is the spatial control of oxygen afforded by simply varying placement of the microcapsules. To demonstrate that the microcapsules can be used to establish spatial oxygen gradients, we utilized a bioprinter to control the distribution of glucose oxidase microcapsules. A concentric circular disc construct was bioprinted for this purpose (Fig. 5*A*). The concentric circular disc consisted of a center disc (radius of 0.5 cm) containing 30 U/mL glucose oxidase microcapsules suspended in a GelMA-based bioink, which served as the oxygen sink. This disc was surrounded by blank GelMA bioink, forming a large annulus with a radius of 2 cm (height = 3 mm). To assess the spatiotemporal patterning of oxygen concentration within the bioprinted disc, we measured the oxygen distribution along the bioprinted construct's radius at a 5-mm interval with an oxygen probe. First, we aimed to determine the temporal dynamics to establish an equilibrium oxygen gradient along the radial axis of the bioprinted disc, which resulted from an influx of oxygen from the surrounding environment (inside a 37 °C and 5% CO_2 incubator) and oxygen scavenging activities by glucose oxidase microcapsules printed in the center of the disc. Excess culture medium (30 mL) was added to ensure that glucose concentration was not limiting the oxygen scavenging activity of the microcapsules. We observed that the oxygen distribution within the disc achieved equilibrium after ~5 h, consistent with our model (Fig. 5*B* and *SI Appendix*, Fig. S8*A*). The equilibrium oxygen concentration gradient in the bioprinted disc ranged from 1.4 ± 0.2% oxygen (oxygen partial pressure in equilibrium with water) at the center of the disc (r = 0 mm) to 19.4 ± 0.5% at the edge (r = 15 mm). The oxygen levels increased along the radius of the disc, where we noted an equilibrium oxygen level of 5.3 ± 1.0% at r = 5 mm and 14.9 ± 1.3% oxygen at r = 10 mm. These experimental data corroborate with our computational simulation model that accounted for diffusion and glucose oxidase reaction kinetics to establish oxygen concentration gradient (Fig. 5 *C* and *D*). Both the experimental data and the simulation model reached ~1% oxygen at the center of the disc after 1 h (Fig. 5 *C* and *D*). There was also good agreement in the concentration gradient profiles of the 1-, 3-, and 5-h time points. However, there was a difference in the 24-h concentration profile, with the computational model overestimating the oxygen level at 5 mm and underestimating at 15 mm (Fig. 5*D*). This is likely due to the resolution of the DO probe used.

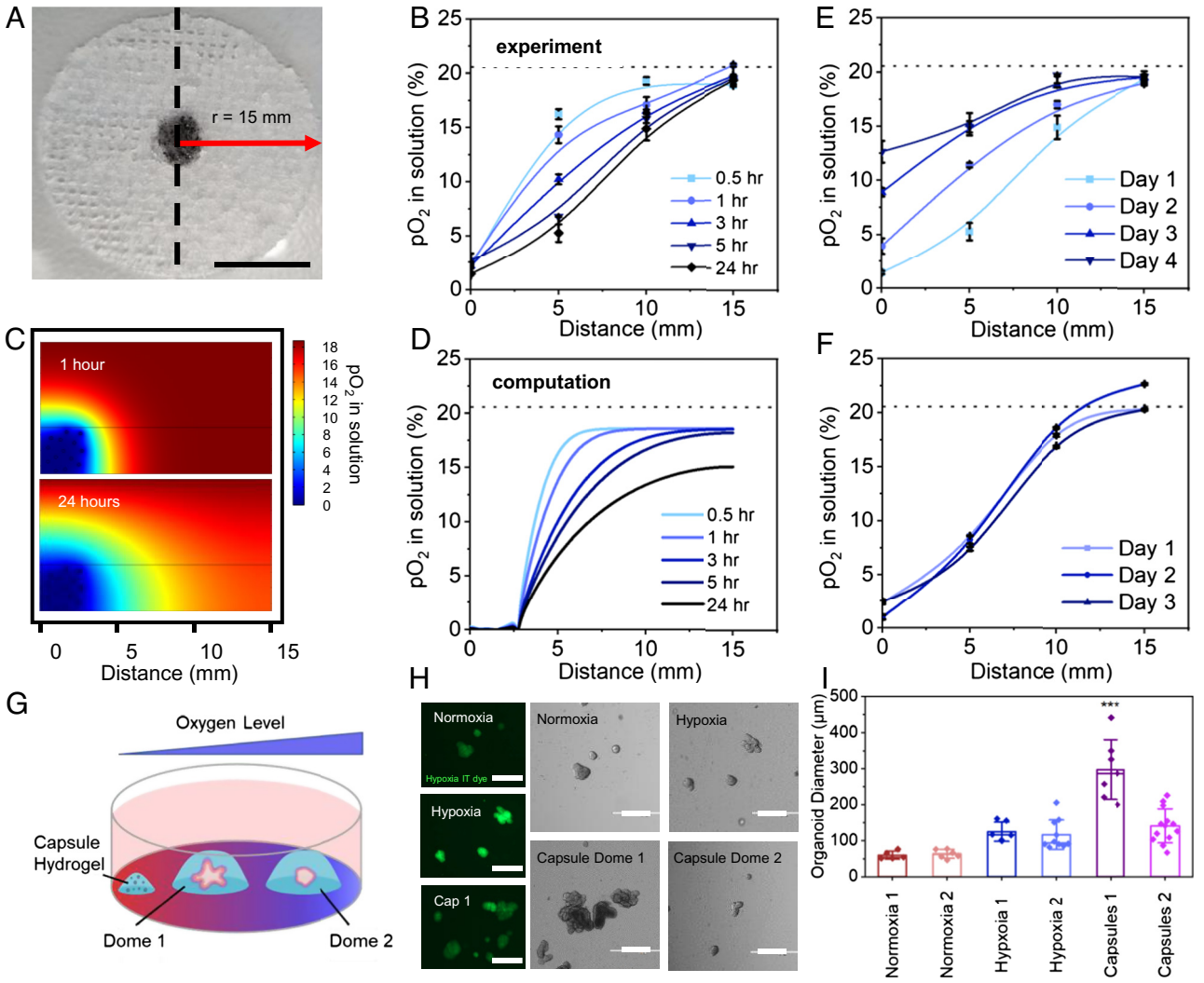

Fig. 5. Spatial control of oxygen directs organoid morphogenesis. (*A*) Blank GelMA C hydrogel is printed as a disc with 0.5-cm internal and 2-cm external radius. Same hydrogel with suspended glucose oxidase microcapsules was dispensed into the center to generate a source–sink disc pattern. (Scale = 1 cm.) (*B*) Bioprinted disc with excess culture media in a cell culture incubator. Oxygen levels measured along the radial direction, r, from the disc center at 5-mm intervals for up to 1 d. (*C*) Computational simulations (COMSOL) modeling of hydrogels in media with loaded capsules after 1 h (*Top*) or 24 h (*Bottom*). (*D*) Plot of computationally modeled oxygen partial pressures in solution that mimics geometry of the bioprinted disc. (*E*) Oxygen distributions of bioprinted disc incubated in 30 mL of cell culture media for 4 d. No media change was performed. (*F*) Oxygen distribution of bioprinted disc incubated in 30 mL cell culture media with daily culture media change. (*G*) Schematic of capsules loaded in a gel droplet near two Matrigel domes at varied distances. (*H*) Optical images intestinal organoids in Matrigel domes that are exposed to varied levels of hypoxia (*Right*), and fluorescent images of intestinal organoids stained with a hypoxia IT dye (*Left*). (*I*) Plot of organoid diameters as a function of which Matrigel dome and oxygen conditions they were in. [Scale bars, 1 cm (*A*), 500 μm (*H*).] Data are presented as average of n > 3 repeats with SD. ***$P < 0.001$, ANOVA. Error bars represent SD.

Next, we evaluated how long the oxygen concentration gradient can be maintained. It was noted that the concentration gradient profile could not be maintained when we incubated the bioprinted disc for 4 d without any medium change. By day 3, the oxygen level at the center of the disc was observed to be at 8.9 ± 0.5%, which was sixfold higher than that in day 1 (1.4 ± 0.2% oxygen) (Fig. 5*E*). This was likely attributed to a decrease in glucose oxidase activity in the microcapsules over the 96 h period. Given that glucose is a key substrate of glucose oxidase, prolonged incubation without medium change likely caused glucose depletion and consequently resulted in a loss of oxygen scavenging activity. With daily replenishment of culture medium, the oxygen concentration gradient could be consistently maintained (Fig. 5*F*). Therefore, we show that by patterning the microcapsules at discrete locations, an oxygen concentration gradient can be readily established under a normal atmospheric condition in a standard cell culture incubator. This is not achievable with commonly used hypoxic incubators, which regulate oxygen concentration at a single uniform level. Hence, combining bioprinting with the oxygen scavenging microcapsules can potentially provide a simple and scalable avenue to mimic physiologically relevant oxygen gradients within a single experiment (45).

Intestinal stem cells are naturally adapted to function in a low-oxygen microenvironment (1 to 3%), leading to better growth in low-oxygen conditions. To evaluate the effect of microcapsule-mediated oxygen gradient on the growth of intestinal tissues, we passaged and seeded intestinal organoids in well plates which were maintained under normoxia (in a 5% CO_2, 21% O_2 incubator) but subjected to an oxygen gradient that was created by depositing a microcapsule loaded hydrogel disc (10 wt. % GelMA) to one side of the well. The microcapsule disc composition is 2 mg/mL corresponding to 25 U of loaded enzyme. This allowed for the creation of a distinct oxygen gradient within the same well. Next, two 10 μL Matrigel/organoid droplets were created within each well. One of the droplets (Dome 1) was positioned near the microcapsule (<5 mm),

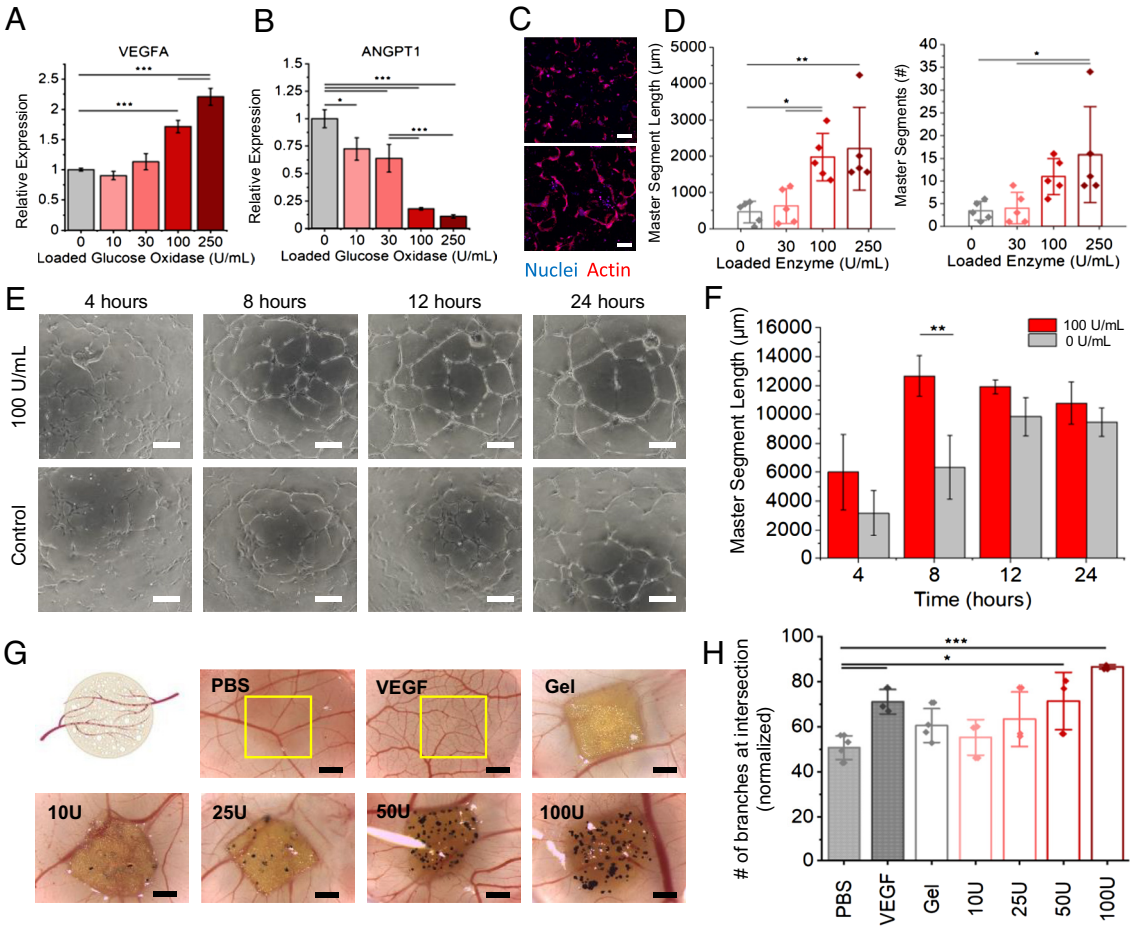

Fig. 6. Effect of hypoxic capsules on endothelial cells. Plots of relative expression of VEGFa. (*A*) and ANGPT-1 (*B*) for HUVECs in microgel suspensions with varied amounts of hypoxic capsules for 24 h. Plots normalized to GAPDH. (*C*) Confocal z-stack projections of HUVECs (5×10^6 cells per mL) stained with Hoechst (nuclei, blue) and phalloidin (actin, red) after 5 d in culture in microgel suspensions (10 wt%, 0.5% filler) with or without 2 vol% of glucose oxidase capsules (100 U/mL, 6,000 U/mL catalase). (*D*) Plots of master segment length (*Right*) and number (*Left*) and lengths for control and glucose oxidase capsule conditions calculated using the angiogenesis analyzer plugin for ImageJ. (*E*) Bright-field images of HUVEC tubulogenesis over the course of 24 h. (*F*) Analysis of master segment length from the tubulogenesis assay. (*G*) Dissecting microscope images of representative CAM assay egg embryos after 4 d of incubation with or without microgel suspensions loaded with glucose oxidase capsules. (*H*) Quantification of the number of interacting branching points from the CAM assay. [Scale bars, 50 μm (*C*), 100 μm (*E*), and 500 μm (*G*).] *$P < 0.05$, **$P < 0.01$, and ***$P < 0.001$, ANOVA. Error bars represent SD.

whereas the second droplet (Dome 2) was positioned at the extreme end of the well, furthest away from the microcapsules (~10 mm) (Fig. 5*G*). This allowed for the comparison of the effect of the oxygen gradient on the growth and morphology of the gut organoids as a function of spatial distance to the hypoxia source. Controls were established by culturing the intestinal organoids in the same setup with a sham disc (no microcapsules) in a 2% O_2 hypoxic incubator, and a 21% normoxic incubator.

After 48 h, organoid size and proliferative ability (evidence as branching and budding) increased with proximity to the microcapsule disc. Organoids grown in the well with 25 U microcapsule disc had a 630% increase in size compared to untreated controls ($P < 0.0001$) (Fig. 5 *H* and *I*). The size of the organoids grown in close proximity to the 25 U capsule reservoir (<5 mm; <5% O_2) was larger than those cultured far from the capsule reservoir (~10 mm; <15% O_2) which was comparable to the size of the positive control organoids grown in the hypoxic incubator (static 2% O_2) (Fig. 5*I*). Under microcapsule conditions, organoids in Dome 1 were 300% larger than those in Dome 2 ($P < 0.001$) and formed significant budding and branched structures. When staining the organoids in all conditions with a hypoxic dye (ImageIT), there was elevated signal in the organoids grown in the hypoxic chamber and when cultured with microcapsules (Fig. 5*H*). Additionally, all hypoxic conditions led to enhanced growth compared to normoxic culture conditions, and there was no difference in size between Dome 1 and Dome 2 in control organoids grown under hypoxia or under normoxia (blank disc; no microcapsules). Together, these results demonstrate how microcapsules can regulate hypoxia with spatial control, leading to enhanced proliferation with evidence for increased growth characteristics compared to hypoxic chambers.

A hypoxic intestinal stem cell microenvironment can have a significant impact on the growth of organoids (46). The intestinal stem cells are responsible for maintaining the intestinal epithelium and are key for the renewal and repair of the gut lining. These cells are located in a niche within the gut, where they are exposed to low oxygen levels (47). In hypoxic conditions, the activation of various signaling pathways, such as the HIF1-α pathway, can regulate cellular metabolism and increase the resistance of cells to oxidative stress, leading to enhanced survival and proliferation of the stem cells (48). This can result in an increased number of stem cells and an improved capacity for self-renewal, which can enhance the growth of the organoids. Furthermore, hypoxia can also influence the expression of various genes involved in cellular metabolism, cellular signaling, and angiogenesis, leading to changes in the cellular behavior of the stem cells that can promote their survival and growth. This can result in an improvement in the quality and size of the organoids, as well as an increased branching pattern,

which is indicative of their growth and proliferation capacity (46). The hypoxic microenvironment of gut has a significant impact on the microbiome as many gut bacteria are anaerobic and require low oxygen levels to grow and thrive. By maintaining a hypoxic environment for the cultivation of gut organoids, the microorganisms that are associated with the gut can be better replicated, which can lead to a more accurate representation of the gut microbiome (49). This highlights the importance of maintaining a hypoxic environment for the cultivation of organoids to achieve optimal growth and function and to mimic the native microenvironment of the gut. These results demonstrate how using oxygen-modulating microcapsules can mimic gut organoid morphogenesis comparable to what is achieved using a hypoxic chamber. By spatially controlling the number and activity of capsules, we were able to locally tune and establish hypoxic gradients, providing the ability to direct different activities spatially within a single experiment.

1.5. Hypoxic Microcapsules Induce Angiogenesis Signaling In Vitro and In Vivo. It is well understood that oxygen levels play a role in endothelial cell signaling pathways (50). Under low oxygen tension, endothelial cells are driven to undergo angiogenesis to create more vessel structures to supply more oxygen. This has been previously demonstrated using hydrogels with oxygen-reducing enzymes tethered to the hydrogel backbone (11). Here, we aimed to measure the effect of hypoxia on vascular endothelial cells using several systems to demonstrate the microcapsule platform's versatility. First, HUVECs were seeded in GelMa microgel suspensions (0% filler, 5×10^6 cells per mL), as a model biofabrication approach, with varied concentrations of glucose oxidase–loaded capsules and cultured for 24 h before snap-freezing the gels and collecting cellular mRNA. RT-qPCR analysis showed an upregulation in vascular endothelial growth factor a (VEGFa) levels with increasing levels of hypoxia, with a twofold difference for the 250 U/mL condition compared to the control condition (Fig. 6*A*) ($P < 0.0001$). There was a simultaneous decrease in Angiopoietin 1 (ANGPT-1) by 10-fold (Fig. 6*B*) and no statistical difference in MMP1 gene expression (*SI Appendix*, Fig. S12*A*). Previous work has demonstrated that hypoxia induces an upregulation in VEGFa and a downregulation in ANGPT-1 in human endometrial cells (51). This is in contrast to other literature showing an upregulation of ANGPT-1 in vascular cells (11), and pericytes under hypoxic conditions (52). Park et al. have shown that this upregulation can be acute and transient (53). The role of ANGPT-1 is primarily vascular protective, preventing endothelial cell death and preserving the structural integrity of vasculature (54). It is possible that in the first 24 h, the dispersed cells increase VEGFa expression due to hypoxia but without the paracrine mechanism that is vascular protective.

To test whether our endothelial cells would still undergo angiogenesis in this system, the previous experiment was repeated but allowed to proceed for 5 d. After 5 d, HUVECs in enzyme capsule-loaded conditions (100 and 250 U/mL glucose oxidase) began to form interconnected tubes (Fig. 6*C* and *SI Appendix*, Fig. S13*A*). For quantification, the angiogenesis analyzer tool in ImageJ was used (*SI Appendix*, Fig. S13*B*). When comparing the two conditions, the 100 and 250 U/mL conditions had 430% and 470% increased master segment length (0 to 100: $P = 0.019$; 0 to 250: $P = 0.0070$) and 320% and 460% more master segments, respectively (0 to 100: $P = 0.227$; 0 to 250: $P = 0.022$). However, when measuring the average branch length (*SI Appendix*, Fig. S12*B*), as well as the mesh area (*SI Appendix*, Fig. S11*C*), there was a trend suggesting that the 100 U/mL had thicker, and thus, healthier vessels, which matches the qualitative observations from the confocal images (*SI Appendix*, Fig. S13*A*).

To further confirm these results, a tubulogenesis on Matrigel assay was performed using the 0 U/mL and 100 U/mL capsule conditions (Fig. 6*E*). These results demonstrated a temporal response to hypoxia, where the hypoxic condition reached its maximum master segment length (Fig. 6*F*), number of master segments (*SI Appendix*, Fig. S12*D*), and number of master junctions (*SI Appendix*, Fig. S12*E*) 4 h earlier than the control conditions. These differences abated by 24 h as is expected with endothelial tubulogenesis experiments on Matrigel. As a final confirmation of the effect of hypoxia in vivo, we ran a chick chorioallantoic membrane (CAM) assay, a well-established in vivo angiogenesis assay. Here, microgel suspensions were made with varied concentrations of capsules, that contain 100 U/mL of glucose oxidase, and were placed onto the CAM of developing chicken embryos. After 4 d of sample exposure, the number of branches intersecting the edge of the gels was analyzed (Fig. 6*G*). No statistical differences were found between the PBS control and the gels loaded with 0, 10, or 25 U/mL enzyme capsules (Fig. 6*H*). However, there was a significant difference between the PBS and the 50 and 100 U/mL conditions (PBS – 50: $P = 0.02$; PBS – 100: $P = 0.0002$). Furthermore, the 100 U/mL condition enhanced angiogenesis with 43% and 22% more intersecting vessels relative to the 0 U/mL gels and the VEGF positive control, respectively. Overall, these data suggest that hypoxia-induced upregulation of VEGFa leads to angiogenesis signaling in 2D, 3D, and in ovo models. However, we cannot discount the possibility that microcapsules are exerting an influence on other processes like inflammation. Nevertheless, the ability to fine-tune the concentration of capsules and enzyme allows for a robust way to investigate subtle changes in the levels of oxygen tension and the influence on neovascularization and angiogenesis.

2. Conclusions

This work demonstrates an approach for spatiotemporal control of hypoxic conditions in virtually any cell culture system. The microcapsule system enables high loading of enzymes with prolonged shelf life and maintenance of activity, which allows for control of hypoxia in cell culture for several weeks. Tuning the capsule concentration or initial enzyme concentration allows for fine control over oxygen levels across a 3D cell culture, and across different samples in a well plate, toward integration in high-throughput assays. Hypoxic conditions were shown to attenuate MSC EV output, as well as modulate the growth characteristics of cancer cells and spheroids. Spatial control of capsule distribution fostered gradient behavior, which demonstrated spatiotemporal control of intestinal organoid morphogenesis. Hypoxic capsules also promoted an upregulation in endothelial VEGFa which led to enhanced angiogenesis signaling in 2D, 3D, and in ovo models. This advance could transform body-on-a-chip devices, where variable oxygen levels can be precisely tuned to different tissues across a single device, something that is not currently possible. This approach can also be adapted to nanozymes, other enzyme systems, or gas-releasing hydrogels for use in a broad range of applications. The flexibility of the microcapsule format provides scope for use as an injectable biomaterial or reservoir for inclusion in topical treatments and gel-based bandages, where gas attenuation may have clinical utility (e.g., wound healing). In addition to these practical applications, we anticipate this system will provide a basis for future work investigating the role of oxygen deprivation on cell signaling pathways and functional cellular outputs.

3. Materials and Methods

3.1. Gelatin Microcapsule Synthesis. For empty capsules, type B gelatin (bloom strength 300, Sigma) was dissolved at 10 wt% in 1× PBS in a 40 °C water bath (75 mL oil). For loaded capsules, a 20 wt% solution of gelatin was dissolved, and it was mixed 1:1 with a solution containing the cargo. The gelatin solution (2 mL) was pushed through a 0.45-μm filter into an oil bath (olive oil) under constant stirring at 38 °C. After 10 min of equilibration, the oil bath was cooled to 10 °C, using a surrounding ice bath, and left to stabilize for 30 min. Hexane (25 mL) was subsequently added and left to stir for 10 min before the microgels were decanted off into centrifuge tubes. The particles were left to settle for 30 min prior to 4 washing steps with hexane. The particles were agitated in the hexane solution and quickly pipetted onto a 25-μm nylon filter over Kim wipes in a fume hood to let the hexane dry off. A spatula was used to spread out the particles on the filter to ensure all hexane was evaporated. Once hexane free, the particles were placed into a centrifuge tube again and resuspended in a Tris-HCl buffer (0.1M, pH 8.5, 10 mL). Dopamine hydrochloride was added (final concentration of 10 mg/mL), and the tube was covered with a Kim wipe to allow oxygen exchange. The tube was then placed on an orbital shaker at 300 rpm for the specified time. The particles were then washed with 1X PBS four times and stored until further use. For size characterization, uncoated particles were placed onto a glass slide and imaged under an optical microscope. One hundred particles were imaged across 7 images, and the diameters were measured using ImageJ.

3.2. Encapsulation Efficiency and Maximal Loading. To quantify encapsulation efficiency, the capsule synthesis procedure was followed [loaded with 10-, 40-, or 250-kDa FITC-dextran cargo (20 μg/mL)] until just before adding in the dopamine. The particles were then placed on the orbital shaker for 4 h to simulate the time prior to a stable coating forming on the surface of the microgels. Microgels were then weighted out and dissolved at 37 °C in 1× PBS to extract the contents. The contents were then measured using a fluorescence spectrophotometer with a laser excitation at 488 nm (Cary Eclipse). The emission at 517 nm was plugged into a line of best fit from a standard curve to calculate the concentration of dextrans in a solution. For maximal BSA loading, the same procedure was followed expect the gelatin particles were loading with 100 mg/mL of BSA and 125 μg/mL of fluorescent FITC-labeled BSA. A separate standard curve for FITC-BSA was produced to create a line of best fit.

3.3. Cell and Organoid Culture. All cell cultures were performed using aseptic techniques inside a sterile class II biological safety cabinet. All cells were cultured inside an incubator at 37 °C with a 5% CO_2 and 100% humidity atmosphere. All cells used in this study were between the passages 2 to 13. The media used for each cell line are described in *SI Appendix*, Table S1. Media changes were performed every 2 d. The adipose-derived stem cells (ADSCs), B16F10, MCF-7, MDA-MB-231, and A375-P cells were all passaged when a confluency of 80 to 90% was reached. HUVECs were passaged at 70 to 80% confluency. For all cell lines, 0.25% trypsin-EDTA was used for detachment.

Adult stem cell–derived intestinal organoids were sourced from molecular and integrative Cystic Fibrosis Biobank (Sydney Children's Hospital Ethics Review Board; HREC/16/SCHN/120). Organoids were established from intestinal crypts isolated from four to six rectal biopsies (as previously described) (47). Briefly, isolated crypts were seeded in 70% Matrigel (growth factor reduced, phenol free; Corning 356231) at a density of ~10 to 30 crypts in 10 μL Matrigel droplets. IntestiCult Organoid Media (STEMCELL 06010) were supplemented with a cocktail of antibiotics. Cryopreserved organoids were cultured for 7 d with IntestiCult Organoid Media (STEMCELL 06010). They were then dissociated and seeded in separate culture plates. One plate was cultured in a trigas incubator (37 °C, 5% CO_2, 2% O_2, hypoxic), while the other plate was cultured in a conventional incubator (37 °C, 5% CO_2, 21% O_2; normoxia). For organoids cultured in normoxia, an oxygen gradient was created in each culture well by depositing a microcapsule disc to one side of the well. To prepare these discs, 1,000 U/mL microcapsules were loaded into 30 μL GelMa (10 wt%) droplets at 0, 2, 5, and 20 mg/mL. These discs were then placed into the well plate on top of a small 5 μL droplet of uncross-linked Matrigel such that the disc is anchored once the droplet cures in the incubator.

3.4. Immunofluorescence Staining and Tissue Clearing. Clearing solutions were prepared as described previously with minor modifications (41). CUBIC 2 solution was prepared by mixing 50 wt% sucrose, 25 wt% urea, and 10 wt% triethanolamine with Deionized (DI) water at 55 °C until also fully dissolved. Microgel suspensions were fixed using 4 wt% paraformaldehyde (PFA) for 1 to 4 d at room temperature to ensure full penetration of PFA into thick constructs. The gels were then rinsed with 1× PBS followed by 3 1× PBS washes at 2- to 4-h intervals. Afterward, the gels were incubated in 0.5 wt% triton overnight before repeating the same wash procedure. The staining for all gels was performed using the dyes and antibodies in *SI Appendix*, Table S2. The gels were washed with 1× PBS three times after both primary and secondary staining before the addition of the CUBIC 2 clearing solution for 1 to 4 d. All confocal imaging was performed with a Zeiss LSM 800. A 10× objective with a 2.5-mm working distance was used to see deeper into the samples. Samples were coated with clearing 2 solutions throughout the duration for the imaging to prevent drying.

3.5. Glucose Oxidase Activity Characterization. Glucose oxidase activity was characterized by using the glucose oxidase activity assay kit according to the manufacturer's protocol. Briefly, glucose oxidase was first dissolved to 20 mg/mL (2,000 U/mL) in a 50 mM sodium acetate buffer at a pH of 5.0. The enzyme was mixed 1:1 with a 20 wt% gelatin solution to make microcapsules that were coated for 24 h. Two other microcapsules were then synthesized: one with 20% as much glucose oxidase and one with no glucose oxidase. The capsules were then placed on 25-μm nylon filters, to remove excess water, and were weighed into an Eppendorf tube. The particles were then resuspended to 20 mg/mL in the GOx buffer solutions from the kit. Then, 50 μL of the capsule buffer solution was added to 4 different wells in a 96-well plate, along 4 wells for blanks, and 5 wells for the standard curve. The plate was then placed into a plate reader (CLARIOstar Plus) set to 37 °C to warm up. Finally, 50 μL of the kit working solution was added to each well, and measurements were taken every 3 min for 45 min in total. Unused microcapsules were then stored in 4 °C for 1 mo, with new measurements taken on days 2, 7, 14, and 21.

3.6. Seeding Cells with Glucose Oxidase and Catalase Microcapsules. For fixed cell experiments, glucose oxidase capsule-laden microgel suspensions were prepared by the same method used in 2.15. For cancer cell response, microgel suspensions were loaded with A375-P (1×10^6 cells per mL) and cultured for 1 and 7 d. Cells were subsequently fixed and stained with Hoechst, phalloidin, and HIF1-α antibody. The images were subsequently taken on a Zeiss LSM 800 confocal and imaging (100-μm z stack with 2-μm slices). Aggregate size analyses were performed in ImageJ. Briefly, the actin cytoskeleton of aggregates was thresholded and masked, and the Analyze particles plugin was used to calculate the average aggregate size per replicate.

For the ADSC response, microgel suspensions (medium, 10 wt%, 1% filler) were loaded with 2 vol% microcapsules (0, 10, 25, or 100 U/mL glucose oxidase with a 1:60 ratio of catalase) and 1×10^6 ADSCs per mL. For images, 100-μm z stacks with 2-μm slices were taken. To calculate mean gray value intensities, the phalloidin channel was used to create ROIs of cell boundaries, and then, these ROIs were applied to the HIF1-α channel to achieve the mean gray of HIF1-α staining per replicate region. For cell counting, the nuclei were thresholded and counted via the analyze particle's function, and HIF1-α expressing cells were counted manually.

3.7. Statistical Analysis. All whiskers in box plots are one SD. For the particle size study, 100 different particles were used. Four replicates were used for the permeability study, and 3 replicates used per condition for the encapsulation efficiency study. Five replicates were used for the BSA capsule stability study, as well as the maximal BSA loading test. For 3D printed line fidelities, 8 separate lines were used, with the diameter averaged across 6 different points along the line. Quadruplicates were used for the glucose oxidase activity studies and triplicates for the DO tests for the capsules. Triplicates were used for the live dead studies. Quadruplicates were used for all ADSC studies, triplicates were used for the A375 studies, and six replicates were used for the breast cancer studies. No replicates were performed for the western blots. Five replicates were used for all HUVEC studies, and 3 eggs were used for each replicate in the CAM assay. Triplicates were used in the MitoSOX study and the irradiation model test. Statistical significance was determined using a one-way ANOVA with Tukey's post hoc HSD analysis.

Differences were considered significant when $P < 0.05$. Statistical significance was highlighted in figures with the following convention: $*P < 0.05$, $**P < 0.01$, $***P < 0.001$, and $****P < 0.001$.

Data, Material, and Software Availability. All data are included within the main and *SI Appendix*.

ACKNOWLEDGMENTS. This work was supported through funding from the National Health and Medical Research Council (K.A.K.: APP1185021; S.A.W.: APP1188987), the Australian Research Council (K.A.K.: DP210103654; Y.-C.T.: FT180100157 and DP200101658), and the National Cancer Institute of the NIH grant (K.A.K.: R01CA251443). Portions of this paper were developed from the thesis of T.G.M. We acknowledge the help and support of staff at the Katharina Gaus Light Microscopy Facility and the Biological Specimen Preparation Laboratory of the University of New South Wales (UNSW) Mark Wainwright Analytical Centre.

Author affiliations: [a]School of Materials Science and Engineering, University of New South Wales, Sydney, NSW 2052, Australia; [b]School of Chemistry, University of New South Wales, Sydney, NSW 2052, Australia; [c]Graduate School of Biomedical Engineering, University of New South Wales, Sydney, NSW 2052, Australia; [d]School of Mechanical, Medical and Process Engineering, Queensland University of Technology, Brisbane, QLD 4000, Australia; [e]Centre for Biomedical Technologies, Queensland University of Technology, Kelvin Grove, QLD 4059, Australia; [f]Max-Planck Queensland Centre, Queensland University of Technology, Kelvin Grove, QLD 4059, Australia; [g]School of Biomedical Sciences, University of New South Wales, Sydney, NSW 2052, Australia; [h]Molecular and Integrative Cystic Fibrosis Research Center, University of New South Wales, Sydney, NSW 2052, Australia; [i]Australian Centre for NanoMedicine, University of New South Wales, Sydney, NSW 2052, Australia; and [j]Centre for Microbiome Research, Queensland University of Technology, Woolloongabba, QLD 4102, Australia

1. M. H. Kim, S. D. Green, C. C. Lin, H. Konig, Engineering tools for regulating hypoxia in tumour models. *J. Cell Mol. Med.* **25**, 7581–7592 (2021).
2. Q. Ke, M. Costa, Hypoxia-inducible factor-1 (HIF-1). *Mol. Pharmacol.* **70**, 1469–1480 (2006).
3. M. D. Brennan, M. L. Rexius-Hall, L. J. Elgass, D. T. Eddington, Oxygen control with microfluidics. *Lab Chip* **14**, 4305–4318 (2014).
4. Z. Ivanovic, Hypoxia or in situ normoxia: The stem cell paradigm. *J. Cell Physiol.* **219**, 271–275 (2009).
5. G. D'Ippolito, S. Diabira, G. A. Howard, B. A. Roos, P. C. Schiller, Low oxygen tension inhibits osteogenic differentiation and enhances stemness of human MIAMI cells. *Bone* **39**, 513–522 (2006).
6. T. L. Place, F. E. Domann, A. J. Case, Limitations of oxygen delivery to cells in culture: An underappreciated problem in basic and translational research. *Free Radic Biol. Med.* **113**, 311–322 (2017).
7. J. Muñoz-Sánchez, M. E. Chánez-Cárdenas, The use of cobalt chloride as a chemical hypoxia model. *J. Appl. Toxicol.* **39**, 556–570 (2019).
8. R. Wang, F. Jin, H. Zhong, A novel experimental hypoxia chamber for cell culture. *Am. J. Cancer Res.* **4**, 53 (2014).
9. R. P. Baumann, P. G. Penketh, H. A. Seow, K. Shyam, A. C. Sartorelli, Generation of oxygen deficiency in cell culture using a two-enzyme system to evaluate agents targeting hypoxic tumor cells. *Radiat Res.* **170**, 651 (2008).
10. K. M. Park, M. R. Blatchley, S. Gerecht, The design of dextran-based hypoxia-inducible hydrogels via in situ oxygen-consuming reaction. *Macromol. Rapid Commun.* **35**, 1968–1975 (2014).
11. K. M. Park, S. Gerecht, Hypoxia-inducible hydrogels. *Nat. Commun.* **5**, 1–12 (2014).
12. C. S. Dawes, H. Konig, C. C. Lin, Enzyme-immobilized hydrogels to create hypoxia for in vitro cancer cell culture. *J. Biotechnol.* **248**, 25–34 (2017).
13. S. Mueller, G. Millonig, G. N. Waite, The GOX/CAT system: A novel enzymatic method to independently control hydrogen peroxide and hypoxia in cell culture. *Adv. Med. Sci.* **54**, 121–135 (2009).
14. C. Zhang, Y. Lv, W. Z. Qiu, A. He, Z. K. Xu, Polydopamine coatings with nanopores for versatile molecular separation. *ACS Appl. Mater Interfaces* **9**, 14437–14444 (2017).
15. S. Libertino, V. Aiello, A. Scandurra, M. Renis, F. Sinatra, Immobilization of the enzyme glucose oxidase on both bulk and porous SiO2 surfaces. *Sensors (Basel)* **8**, 5637 (2008).
16. T. G. Molley, T.-T. Hung, K. A. Kilian, T. G. Molley, K. A. Kilian, Cell-laden gradient microgel suspensions for spatial control of differentiation during biofabrication. *Adv. Healthc Mater* **11**, e2201122 (2022), 10.1002/ADHM.202201122.
17. P. R. Baraniak *et al.*, Stiffening of human mesenchymal stem cell spheroid microenvironments induced by incorporation of gelatin microparticles. *J. Mech. Behav. Biomed Mater* **11**, 63–71 (2012).
18. L. A. Johnson, E. W. Lusas, Comparison of alternative solvents for oils extraction. *J. Am. Oil Chem. Soc.* **60**, 229–242 (1983).
19. S. P. Le-Masurier, H. T. T. Duong, C. Boyer, A. M. Granville, Surface modification of polydopamine coated particles via glycopolymer brush synthesis for protein binding and FLIM testing. *Polym Chem.* **6**, 2504–2511 (2015).
20. H. Lee, S. M. Dellatore, W. M. Miller, P. B. Messersmith, Mussel-inspired surface chemistry for multifunctional coatings. *Science* **1979**, 426–430 (2007).
21. B. Yu, D. A. Wang, Q. Ye, F. Zhou, W. Liu, Robust polydopamine nano/microcapsules and their loading and release behavior. *Chem. Commun.* **45**, 6789–6791 (2009).
22. B. S. Kim *et al.*, BSA-FITC-loaded microcapsules for in vivo delivery. *Biomaterials* **30**, 902–909 (2009).
23. Q. He, Z. Guo, Y. Cao, M. Yang, S. Yao, Selective separation of main flavonoids by combinational use of ionic liquid-loaded microcapsules from crude extract of Tartary buckwheat. *Food Chem.* **362**, 130255 (2021).
24. S. Bin Wang, A. Z. Chen, L. J. Weng, M. Y. Chen, X. L. Xie, Effect of drug-loading methods on drug load, encapsulation efficiency and release properties of alginate/poly-L-arginine/chitosan ternary complex microcapsules. *Macromol. Biosci.* **4**, 27–30 (2004).
25. A. v. Ermakov, *et al.*, Influence of heat treatment on loading of polymeric multilayer microcapsules with rhodamine B. *Macromol. Rapid Commun.* **40**, 1800200 (2019).
26. W. Tong, Y. Zhu, Z. Wang, C. Gao, H. Möhwald, Micelles-encapsulated microcapsules for sequential loading of hydrophobic and water-soluble drugs. *Macromol. Rapid Commun.* **31**, 1015–1019 (2010).
27. E. T. da Cruz Almeida *et al.*, Chemical and microbiological characterization of tinctures and microcapsules loaded with Brazilian red propolis extract. *J. Pharm Anal.* **7**, 280–287 (2017).
28. Q. Zhao, B. Li, pH-controlled drug loading and release from biodegradable microcapsules. *Nanomedicine* **4**, 302–310 (2008).
29. J. P. Newsom, K. A. Payne, M. D. Krebs, Microgels: Modular, tunable constructs for tissue regeneration. *Acta Biomater* **88**, 32–41 (2019).
30. A. C. Daly, L. Riley, T. Segura, J. A. Burdick, Hydrogel microparticles for biomedical applications. *Nature Reviews Materials* **5**, 20–43 (2020), 10.1038/s41578-019-0148-6.
31. S. Xin *et al.*, Generalizing hydrogel microparticles into a new class of bioinks for extrusion bioprinting. *Sci. Adv.* **7**, eabk3087 (2021).
32. M. J. Poznansky, T. M. S. Chang, Comparison of the enzyme kinetics and immunological properties of catalase immobilized by microencapsulation and catalase in free solution for enzyme replacement. *Biochim. Biophys. Acta–Enzymol.* **334**, 103–115 (1974).
33. P. C. Nien, T. S. Tung, K. C. Ho, Amperometric glucose biosensor based on entrapment of glucose oxidase in a poly(3,4-ethylenedioxythiophene) film. *Electroanalysis* **18**, 1408–1415 (2006).
34. R. E. Kim, S. G. Hong, S. Ha, J. Kim, Enzyme adsorption, precipitation and crosslinking of glucose oxidase and laccase on polyaniline nanofibers for highly stable enzymatic biofuel cells. *Enzyme Microb. Technol.* **66**, 35–41 (2014).
35. D. B. Kolesky, K. A. Homan, M. A. Skylar-Scott, J. A. Lewis, Three-dimensional bioprinting of thick vascularized tissues. *Proc. Natl. Acad. Sci. U.S.A.* **113**, 3179–84 (2016).
36. L. Fajersztajn, M. M. Veras, Hypoxia: From placental development to fetal programming. *Birth Defects Res.* **109**, 1377–1385 (2017).
37. Z. Tao, R. A. Raffel, A. K. Souid, J. Goodisman, Kinetic studies on enzyme-catalyzed reactions: Oxidation of glucose, decomposition of hydrogen peroxide and their combination. *Biophys. J.* **96**, 2977–2988 (2009).
38. T. G. Molley *et al.*, Heterotypic tumor models through freeform printing into photostabilized granular microgels. *Biomater Sci.* **9**, 4496–4509 (2021), 10.1039/D1BM00574J.
39. L. P. Zhu *et al.*, Hypoxia-elicited mesenchymal stem cell-derived exosomes facilitates cardiac repair through miR-125b-mediated prevention of cell death in myocardial infarction. *Theranostics* **8**, 6163 (2018).
40. J. Zhu *et al.*, Myocardial reparative functions of exosomes from mesenchymal stem cells are enhanced by hypoxia treatment of the cells via transferring microRNA-210 in an nSMase2-dependent way. *Artif Cells Nanomed Biotechnol.* **46**, 1659–1670 (2018).
41. S. Yang, S. Guo, S. Tong, X. Sun, Promoting osteogenic differentiation of human adipose-derived stem cells by altering the expression of exosomal miRNA. *Stem Cells Int* **2019**, 1351860 (2019).
42. M. Guppy, The hypoxic core: A possible answer to the cancer paradox. *Biochem. Biophys. Res. Commun.* **299**, 676–680 (2002).
43. Y. Lou *et al.*, Targeting tumor hypoxia: Suppression of breast tumor growth and metastasis by novel carbonic anhydrase IX inhibitors. *Cancer Res.* **71**, 3364–3376 (2011).
44. E. K. Rofstad, K. Galappathi, B. S. Mathiesen, Tumor interstitial fluid pressure–A link between tumor hypoxia, microvascular density, and lymph node metastasis. *Neoplasia* **16**, 586–594 (2014).
45. B. Muz, P. de la Puente, F. Azab, A. K. Azab, The role of hypoxia in cancer progression, angiogenesis, metastasis, and resistance to therapy. *Hypoxia* **3**, 83 (2015).
46. X. Han *et al.*, Creating a more perfect union: Modeling intestinal bacteria-epithelial interactions using organoids. *Cell Mol. Gastroenterol. Hepatol.* **12**, 769–782 (2021).
47. S. L. Wong *et al.*, Molecular dynamics and functional characterization of I37R-CFTR lasso mutation provide insights into channel gating activity. *iScience* **25**, 103710 (2022).
48. E. L. Lund *et al.*, Differential regulation of VEGF, HIF1α and angiopoietin-1, -2 and -4 by hypoxia and ionizing radiation in human glioblastoma. *Int. J. Cancer* **108**, 833–838 (2004).
49. T. Kumar, R. Pandey, N. S. Chauhan, Hypoxia Inducible Factor-1α: The Curator of Gut Homeostasis. *Front Cell Infect Microbiol.* **10**, 227 (2020).
50. J. D. Loike *et al.*, Hypoxia induces glucose transporter expression in endothelial cells. *Am. J. Physiol.* **263**, C326–C333 (1992), 10.1152/ajpcell.1992.263.2.C326 263.
51. T. Tsuzuki *et al.*, Divergent regulation of angiopoietin-1, angiopoietin-2, and vascular endothelial growth factor by hypoxia and female sex steroids in human endometrial stromal cells. *Eur. J. Obstetrics & Gynecol. Reproductive Biol.* **168**, 95–101 (2013).
52. Y. S. Park *et al.*, Expression of angiopoietin-1 in hypoxic pericytes: Regulation by hypoxia-inducible factor-2α and participation in endothelial cell migration and tube formation. *Biochem. Biophys. Res. Commun.* **469**, 263–269 (2016).
53. Y. S. Park, N. H. Kim, I. Jo, Hypoxia and vascular endothelial growth factor acutely up-regulate angiopoietin-1 and Tie2 mRNA in bovine retinal pericytes. *Microvasc Res.* **65**, 125–131 (2003).
54. N. P. J. Brindle, P. Saharinen, K. Alitalo, SIgnaling and functions of angiopoietin-1 in vascular protection. *Circ Res.* **98**, 1014–1023 (2006).